analytical chemistry

pubs.acs.org/ac Article

Enhanced Electrochemiluminescence of Graphitic Carbon Nitride by Adjustment of Carbon Vacancy for Supersensitive Detection of MicroRNA

Linlei Liu, Yidan Zhu, Haijun Wang, Yue Zhang, Yaqin Chai,* and Ruo Yuan*

Cite This: *Anal. Chem.* 2022, 94, 12444−12451 Read Online

ACCESS | Metrics & More | Article Recommendations | Supporting Information

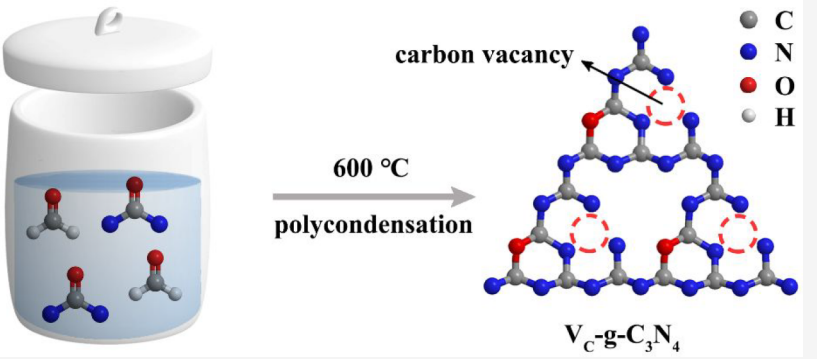

ABSTRACT: Herein, a supersensitive biosensor was constructed by using graphitic carbon nitride with a carbon vacancy (V_C-g-C_3N_4) as an efficient electrochemiluminescence (ECL) emitter for detection of microRNA-21 (miRNA-21). Impressively, V_C-g-C_3N_4 could be prepared by formaldehyde (HCHO)-assisted urea ploycondensation, and the concentration of the carbon vacancy could be controlled by adjusting the dosage of HCHO to improve the ECL performance, in which the carbon vacancy could improve the charge carrier transfer to enhance the conductivity and it also could be used as an electron trap to prevent electrode passivation and facilitate the adsorption of coreactant $S_2O_8^{2-}$ to accelerate its reduction. Compared with original g-C_3N_4, the introduction of carbon vacancies resulted in a significant enhancement of the ECL efficiency of V_C-g-C_3N_4. With the aid of improved cascade strand displacement amplification (IC-SDA), the ECL biosensor realized sensitive detection of miRNA-21 with a low detection limit of 3.34 aM. This successful strategy promoted the development of g-C_3N_4 in the ECL field to construct the sensitive biosensor for molecular and disease diagnoses.

INTRODUCTION

The vacancy could adjust the electronic structure, enhance the adsorption and catalytic activity of materials, accelerate the carrier transport rate, and mediate energy transfer, which were widely used in batteries, catalysis, biosensors, and other fields.[1−5] In recent years, graphitic carbon nitride (g-C_3N_4) has gradually been applied in the electrochemiluminescence (ECL) field due to the advantages of adjustable π-conjugated electronic structure, low cost preparation, and excellent biocompatibility.[6−9] However, the low conductivity and electrode passivation resulted in weak ECL intensity and poor stability, which severely limited further development of g-C_3N_4 in ECL.[10−12] In order to solve those problems, nitrogen vacancy and oxygen vacancy were introduced to adjust the electronic structure of g-C_3N_4 for improving conductivity and alleviating electrode passivation, which could enhance the ECL efficiency of g-C_3N_4.[13,14] However, it was difficult to control the concentration of vacancy on g-C_3N_4 due to the randomness of the treatment by inert gas etching, which might hinder the electron transmission to further affect the catalytic performance.[15] Meanwhile, the high binding energies of N atoms and O atoms on the vacancy might make nitrogen vacancy and oxygen vacancy easily disappear with the filling of N and O.[16,17] Therefore, it is urgent to explore a new method to synthesize stable vacancies for improving ECL performance. In this work, carbon vacancy was introduced into g-C_3N_4 (V_C-g-C_3N_4) by a formaldehyde (HCHO)-assisted urea thermal ploycondensation method for the first time to significantly improve ECL efficiency (Scheme 1A).

Herein, with the aid of improved cascade strand displacement amplification (IC-SDA) and V_C-g-C_3N_4 as an ECL

Received: June 8, 2022
Accepted: August 2, 2022
Published: August 29, 2022

https://doi.org/10.1021/acs.analchem.2c02462
Anal. Chem. 2022, 94, 12444−12451

Scheme 1. (A) Synthesis Process of V_C-g-C_3N_4, (B) Construction Process of Electrodes, (C) Improved Cascade Strand Displacement Amplification.

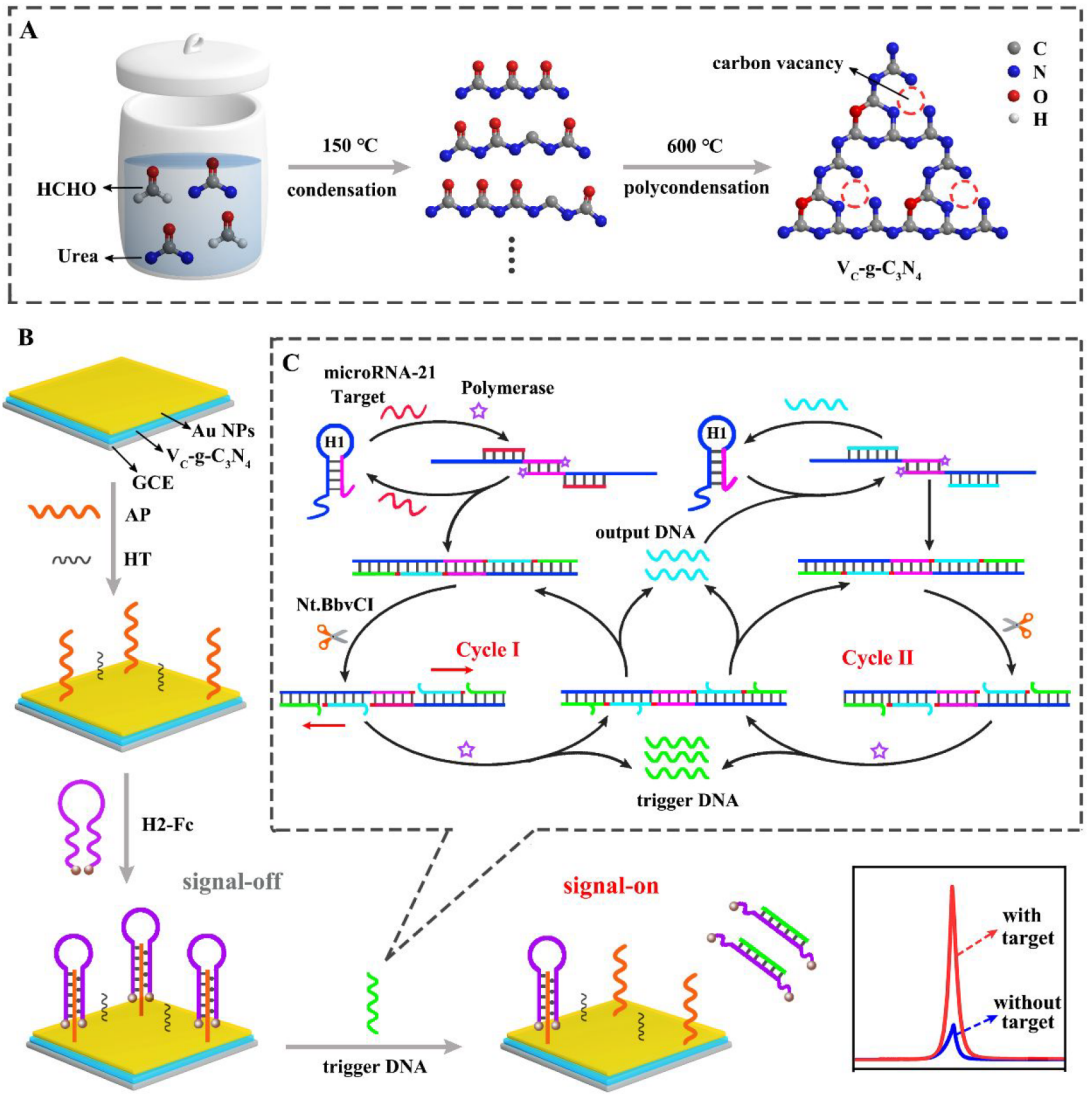

emitter, a supersensitive biosensor was constructed for detection of microRNA-21 (miRNA-21). As depicted in Scheme 1B, first, Au NPs@V_C-g-C_3N_4 was immobilized on the electrode as a signal probe. Then, the capture DNA (AP) was modified on the above electrode. After the quenching probe (H2-Fc) hybridized with AP to form triple-helix structure, Fc was closer to the emitters, resulting in an extremely low ECL signal. Subsequently, the H2-Fc could be far away from the electrode in the presence of the trigger DNA to realize the signal recovery, in which amounts of trigger DNA was obtained after the target microRNA-21(miRNA-21) triggered the process of improved cascade strand displacement amplification (IC-SDA) (Scheme 1C). Compared with the traditional single specific site SDA, the IC-SDA could carry out bidirectional amplification reactions to export the trigger DNA and output DNA that could trigger the second cycle, which greatly improved the signal amplification efficiency. As expected, the prepared biosensor realized the sensitive detection of miRNA-21. Significantly, this work enriched the development of carbon vacancies in ECL and provided a new insight for the detection of disease biomarkers.

EXPERIMENTAL SECTION

Preparation of Emitter. All chemicals involved were analytical grade and have not been further purified. Carbon vacancy-modified graphitic carbon nitride (V_C-g-C_3N_4) was synthesized as follows:[15] 21 g of urea was melted in a crucible at 150 °C, Then, different volumes of 37% formaldehyde (HCHO) were added to form transparent precursors for later calcination polymerization. Then, the transparent precursors should be quickly transferred to a muffle furnace and calcined at 600 °C for 3 h with a heating rate of 5 °C/min. After ultrasonic treatment, the nanosheets were obtained and denoted as V_C-g-C_3N_4-x, where x (5, 15, 30, 40, 50 and 60) was the volume (μL) of HCHO. G-C_3N_4 was synthesized by directly calcining urea in a crucible at 600 °C for 3 h in a muffle furnace.

In addition, Au NPs@V_C-g-C_3N_4 was synthesized according to the following steps:[18] 1 mL of 1 mg/mL V_C-g-C_3N_4 and 10 μL of 0.01 M $HAuCl_4$ were stirred and ultrasonically mixed for 2 h. Then, 25 μL of 0.01 M fresh $NaBH_4$ solution was added and stirred for 20 min. Subsequently, 10 μL of 0.01 M sodium citrate solution was added and stirred for 30 min again. The

https://doi.org/10.1021/acs.analchem.2c02462
Anal. Chem. 2022, 94, 12444−12451

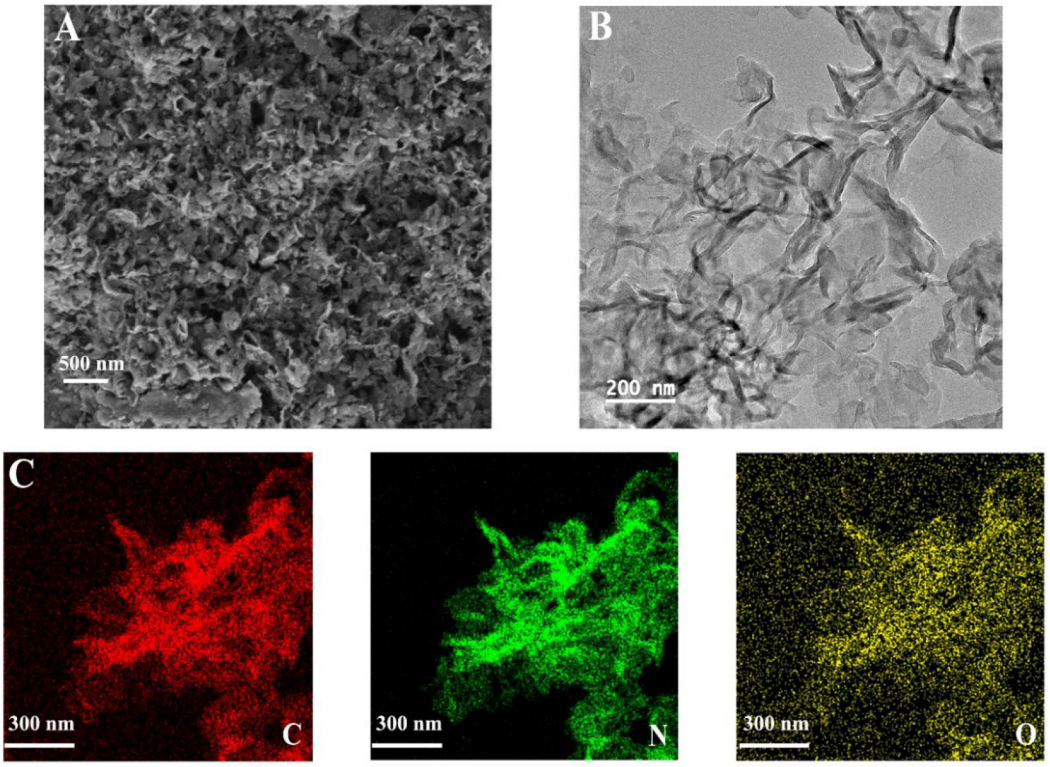

Figure 1. SEM (A), TEM (B) image, and elemental mappings (C) of V_C-g-C_3N_4-50.

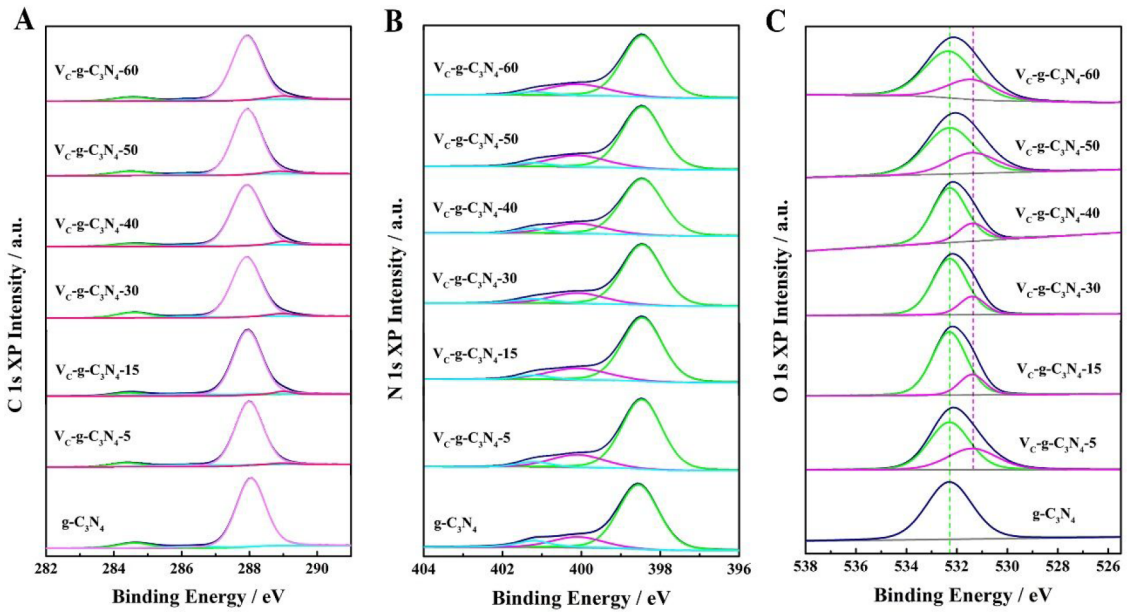

Figure 2. XPS spectra of C 1s (A), N 1s (B), and O 1s (C) for g-C_3N_4 and V_C-g-C_3N_4.

obtained solution was centrifuged and redispersed in 1 mL of water to obtain Au NPs@V_C-g-C_3N_4.

Improved Cascade Strand Displacement Amplification. The amplification process of target circulation is as follows: All DNA and RNA were dissolved in TE buffer containing 12.5 mM Mg^{2+}. First, 10 μM H1 was annealed at 95 °C for 5 min and gradually cooled to RT. Then, 5 μL of 10 μM H1, 15 μL of different concentrations of miRNA-21, 1 μL of 5 U/μL Klenow fragment (3′-5′ exo-), 3 μL of 10 × NEB buffer, 1 μL of 10 U/μL Nt.BbvCI, 2 μL of 10 mM dNTPs, and 3 μL of cutsmart buffer were added and mixed evenly in turn. Subsequently, the solution was reacted at 37 °C for 5 h and thermally inactivated at 80 °C for 20 min to stop the reaction, which could obtain a lot of output DNA. Then, the above solution was cooled to RT and stored at 4 °C for later use.

Construction of ECL Detection Platform. Firstly, the bare GCE should be burnished with 0.3 and 0.05 μm of alumina powder by the literature method.[19] Secondly, 10 μL of 1 mg/mL Au NPs@V_C-g-C_3N_4 was dropped onto the fresh GCE and dried. After that, Au NPs@V_C-g-C_3N_4/GCE was

https://doi.org/10.1021/acs.analchem.2c02462
Anal. Chem. 2022, 94, 12444−12451

incubated with 10 μL of 1 μM AP at 4 °C overnight, and 1 mM HT was used to block the remaining sites. Then, 10 μL of 2 μM H2-Fc was spread on HT/AP/Au NPs@V_C-g-C_3N_4/GCE to form a triplex quenching probe. Finally, 10 μL of output DNA collected from the circulation was added to the above GCE to realize signal recovery. The ECL response was studied by a MPI-ECL analyzer in 2 mL PBS (pH 7.4) containing 2 mM $S_2O_8^{2-}$, where the ECL scanning potential was varied from 0 to −1.6 V, and the photomultiplier tube (PMT) was set at 800 V with a scanning rate of 200 mV/s.

RESULTS AND DISCUSSION

Morphology and Structure Characterization. First, the morphology of V_C-g-C_3N_4-50 was characterized by SEM and TEM. As shown in Figure 1A, V_C-g-C_3N_4-50 had a fluffy flaky stacking structure, and there were many pores between the nanoplatelets. In addition, the lamellar structure of V_C-g-C_3N_4-50 could be clearly seen from the structure of a projection electron microscope. Compared with the simple bulk stacking structure of pure g-C_3N_4, the gas (CO_2 and H_2O) which was generated in the thermal condensation process after adding formaldehyde could avoid the agglomeration of nanosheets and form loose and porous nanostructures.[15] Meanwhile, the element map of TEM showed that there were three elements of C, N, O in V_C-g-C_3N_4-50, and these three elements were uniformly distributed in the structure of V_C-g-C_3N_4-50, in which the oxygen atoms came from molten urea by self-doping during the synthesis process. This result preliminarily verified the successful preparation of the material.

In order to obtain the structural information on V_C-g-C_3N_4, XPS, UV−vis, PL spectrum, FT-IR, and XRD were adopted. The fitted peaks of the C 1s XPS spectrum were shown in Figure 2A. The peaks centered at 284.6, 286.2, and 288.04 eV corresponded to C−C, C−NH_x, and N−C═N in the framework, respectively.[20] However, the V_C-g-C_3N_4 samples had a new weak peak at 288.99 eV, which was attributed to the formation of a C−O bond.[15] From the fitted N 1s XPS spectra exhibited in Figure 2B, there were three peaks located at 401.2, 400.1, and 398.5 eV, which could be ascribed to C−NH_x, N_{3C}, and N−C═N, respectively. The fitted O 1s XPS spectrum was shown in Figure 2C, both the g-C_3N_4 and V_C-g-C_3N_4 samples all showed one peak at 532.2 eV, which was related to the oxygen-containing substances adsorbed on the surface. But the V_C-g-C_3N_4 samples exhibited a new peak at 531.4 eV, corresponding to the formation of C−O−C bonds.[21] From Figure S1A, the FL emission wavelengths of the V_C-g-C_3N_4 samples were about from 448 to 470 nm, and the wavelength was slightly redshifted with the introduction of carbon vacancies. For V_C-g-C_3N_4-50, the position of the emission wavelength showed no remarkable change as the excitation wavelength changed, which indicated that V_C-g-C_3N_4 had no excitation dependence (as shown in Figure S1B). From the FT-IR spectrum in Figure S1C, g-C_3N_4 and V_C-g-C_3N_4 all had similar characteristic peaks. In detail, the sharp peak at 810 cm^{-1}, multiple peaks at around 1200−1700 cm^{-1}, and the broad peak in the range of 3000−3500 cm^{-1}, which corresponded to the breathing vibration of heptazine units, stretching modes of C−N heterocycles, and intermolecular N−H vibration, respectively.[13] As depicted in Figure S1D, g-C_3N_4 and V_C-g-C_3N_4 showed two similar characteristic peaks at 12.9° and 27.6°, corresponding to the (100) and (002) planes,[20] which proved that the introduction of carbon vacancies did not change the primary structure of g-C_3N_4.

ECL Performance of Different Materials. In order to study the different ECL performance between doped and undoped g-C_3N_4, we compared the ECL intensity, ECL emission wavelength, and ECL efficiency of g-C_3N_4 and V_C-g-C_3N_4-50, respectively. As indicated in Figure 3, the ECL

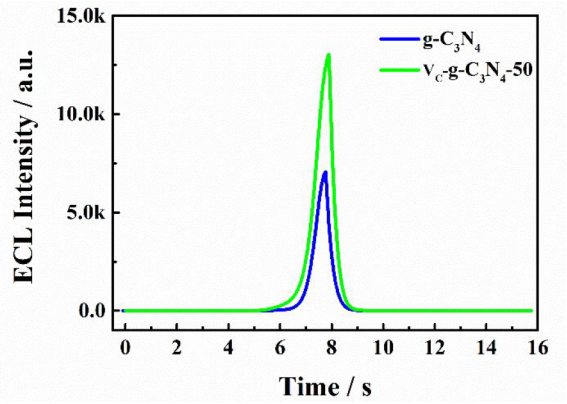

Figure 3. ECL intensity−time curves of g-C_3N_4 and V_C-g-C_3N_4-50.

intensity of V_C-g-C_3N_4-50 was obviously higher than that of g-C_3N_4, which indicated that carbon vacancies could enhance the ECL response of g-C_3N_4. In addition, the ECL efficiency was also an important parameter to measure the ECL performances of materials. As listed in Table S2, it was worth noting that the ECL efficiency (Φ_{ECL}) of V_C-g-C_3N_4-50 was 37.04%, which was about 4.4 times than that of g-C_3N_4 (8.37%). It further proved that carbon vacancies could improve the ECL performance of g-C_3N_4. Finally, we also compared ECL spectra of g-C_3N_4 with different vacancies induced by different contents of formaldehyde. As we can see from Figure 4, the ECL emission wavelength of V_C-g-C_3N_4-50 was at 500 nm, and as depicted in Figure S2, the position of the maximum emission wavelength of V_C-g-C_3N_4-x (x was 5, 15, 30, 40,60) in the ECL spectrum did not change greatly, which corresponded to the slight shift of maximum emission wavelength in the FL spectrum.

To analyze deep insights into the enhancement mechanism of the ECL performance, we compared the band gap, electrochemical impedance spectroscopy (EIS), and differential pulse voltammetry (DPV) of g-C_3N_4 and V_C-g-C_3N_4-50, respectively. As observed in Figure 5A, the introduction of carbon vacancies made the absorption peak of g-C_3N_4 exhibit a redshift. From the UV−vis DRS in Figure 5A, the instinct band gaps calculated by the Kubelka−Munk function were narrowed from 2.82 of pure g-C_3N_4 to 2.7 of V_C-g-C_3N_4-50. In addition, we also compared the reduction peaks of g-C_3N_4 and V_C-g-C_3N_4-50. As depicted in Figure 5C, the reduction currents of g-C_3N_4 and V_C-g-C_3N_4-50 were located at −1.05 and −0.99 V, respectively. According to the literature,[22] the reduction peak corresponded to the energy level of LUMO, so we could speculate that the introduction of carbon vacancies could cause the undershift of LUMO. Finally, EIS was used to evaluate the electrical conductivities of materials. As shown in Figure 5D, the resistance electron transfer (R_{et}) decreased with an increase in the volume of HCHO. This result indicated that the introduction of carbon vacancies in g-C_3N_4 was beneficial to improve electron transfer. Thus, the excellent ECL performance could be attributed to the under-shift of LUMO and narrowing of the band gap.

https://doi.org/10.1021/acs.analchem.2c02462
Anal. Chem. 2022, 94, 12444−12451

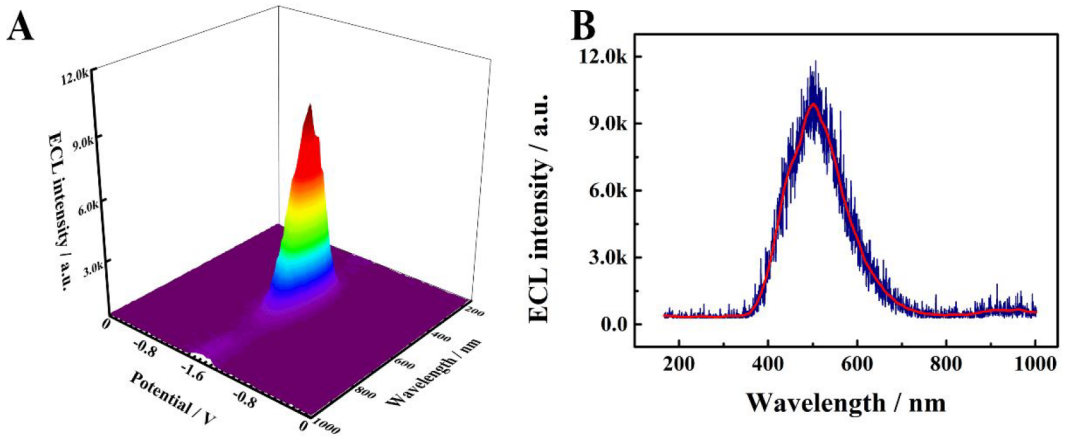

Figure 4. (A) 3D ECL surface image and (B) ECL emission spectrum of V_C-g-C_3N_4-50.

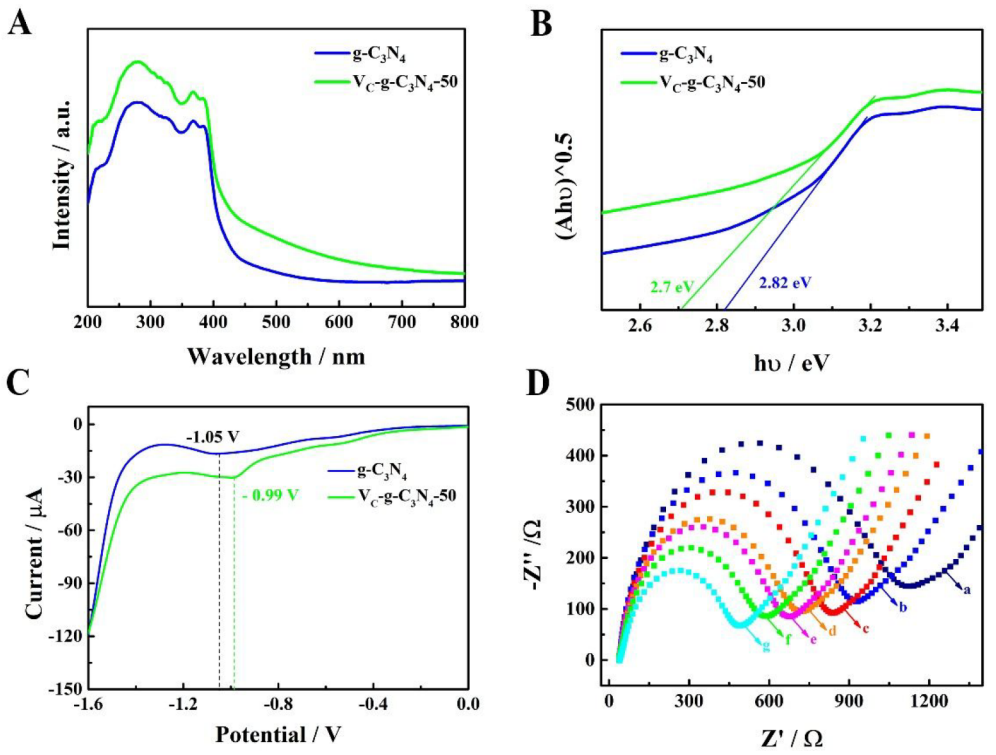

Figure 5. (A) UV−vis DRS, (B) band gaps, and (C) DPV curves of g-C_3N_4 and V_C-g-C_3N_4-50. (D) EIS curves of (a) g-C_3N_4, (b) V_C-g-C_3N_4-5, (c) V_C-g-C_3N_4-15, (d) V_C-g-C_3N_4-30, (e) V_C-g-C_3N_4-40, (f) V_C-g-C_3N_4-50, and (g) V_C-g-C_3N_4-60.

Possible ECL Mechanism. The DPV and ECL measurements were applied to study the ECL emission mechanism of the V_C-g-C_3N_4-50, and the scan potential ranged from 0 to −1.6 V. As shown in Figure 6A, an obvious reduction peak at −1.06 V was observed when V_C-g-C_3N_4-50/GCE was tested in PBS without $S_2O_8^{2-}$ (curve c). In addition, the ECL intensity of V_C-g-C_3N_4-50/GCE was 1818 a.u., attributed to the emission of V_C-g-C_3N_4-50 with dissolved oxygen as the coreactant (Figure 6B, curve c). When the GCE was measured in PBS containing $S_2O_8^{2-}$, a characteristic reduction peak could be observed at about −0.8 V which belonged to $S_2O_8^{2-}$ (Figure 6A, curve b). In addition, when the V_C-g-C_3N_4-50-modified GCE was tested in PBS containing $S_2O_8^{2-}$, there was an obvious reduction peak located at −0.99 V (Figure 6A, curve d), and it showed a much higher ECL intensity than that in PBS (Figure 6B, curve d), which indicated that $S_2O_8^{2-}$ could be saved as a coreactant to accelerate the transformation process from V_C-g-$C_3N_4^{\bullet-}$ to V_C-g-C_3N_4*.

$$S_2O_8^{2-} + e^- \rightarrow SO_4^{\bullet-} + SO_4^{2-} \quad (1)$$

$$V_C\text{-g-}C_3N_4 + e^- \rightarrow V_C\text{-g-}C_3N_4^{\bullet-} \quad (2)$$

$$V_C\text{-g-}C_3N_4^{\bullet-} + SO_4^{\bullet-} \rightarrow V_C\text{-g-}C_3N_4^{*} + SO_4^{2-} \quad (3)$$

$$V_C\text{-g-}C_3N_4^{*} \rightarrow V_C\text{-g-}C_3N_4 + hv \quad (4)$$

Feasibility of Improved Cascade Strand Displacement Amplification. In order to verify the feasibility of improved cascade strand displacement amplification (IC-SDA), polyacrylamide-gel electrophoresis (PAGE) was performed. As shown in Figure 7, lane 1 and lane 2 represent H1 and target miRNA-21, respectively. When the miRNA-21

https://doi.org/10.1021/acs.analchem.2c02462
Anal. Chem. 2022, 94, 12444−12451

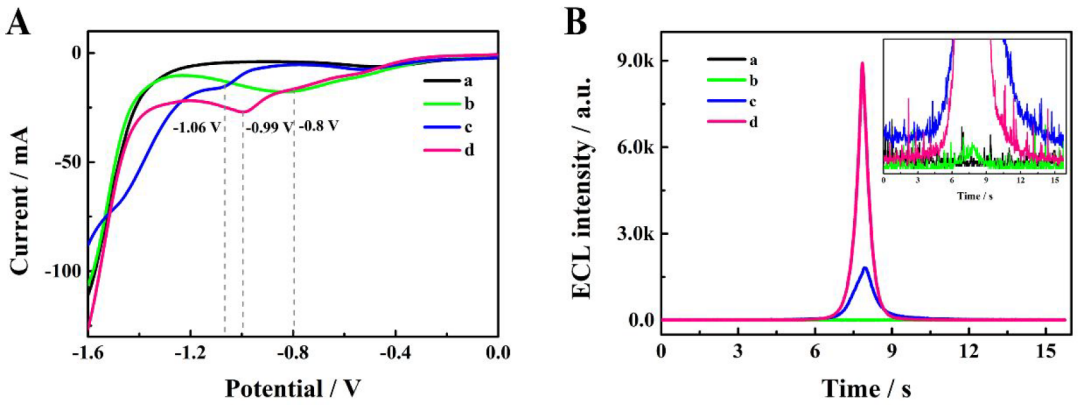

Figure 6. (A) DPV curves and (B) ECL intensity−time curves of bare GCE and V_C-g-C_3N_4-50/GCE in PBS without (a, c) and with (b, d) 2 mM $S_2O_8^{2-}$.

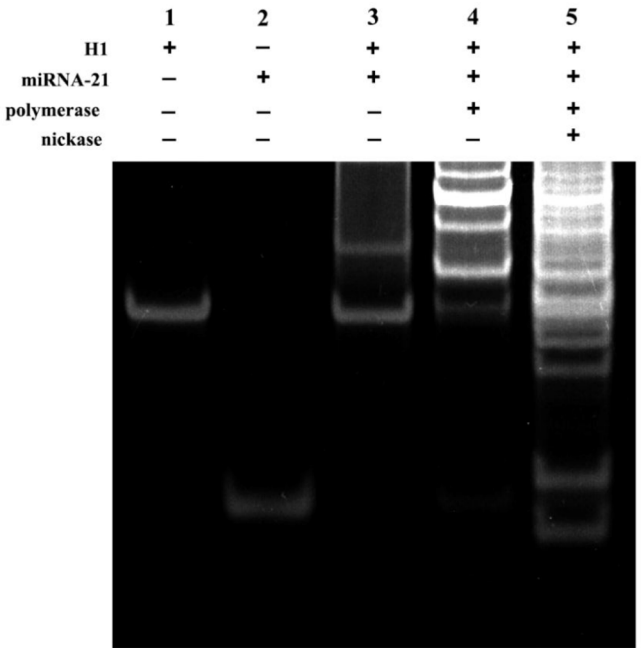

Figure 7. PAGE electrophoresis analysis of miRNA-21 detection by IC-SDA.

opened H1, a band with slow migration appeared (lane 3). Compared with lane 3, a band with slower migration in lane 4 was obtained in the presence of H1, miRNA-21, and a Klenow fragment (3′-5′ exo-). A band with fast migration was shown in lane 5 after the introduction of nickase Nt.BbvCI, which proved that our improved cascade strand displacement amplification strategy was successful.

Analytical Performance of Constructed Biosensor. To evaluate the practicability of the constructed biosensor, we characterized this biosensor assembly process by CV, EIS, and ECL (Supporting Information, Figures S3 and S4). Then, the ECL intensity of the biosensor corresponding to different concentrations of miRNA-21 were evaluated under the selected optimum conditions (Supporting Information, Figures S5 and S6). The ECL signal gradually increased with miRNA-21 concentrations from 10 aM to 1 nM (Figure 8A), and the linear equation was I = 23635.76 + 1251.73 lg c (R = 0.995) with a detection limit of 3.34 aM (Figure 8B). Meanwhile, compared with other detection methods of miRNA-21 (Table 1), this work showed a wider detection range and a lower detection limit, which indicated that this biosensor had a brighter application prospect in cancer marker detection.

In addition, selectivity and stability were two important parameters to evaluate the performance of the biosensor. First, miRNA-let-7a, miRNA-let-7b, miRNA-let-7c, miRNA-155 and miRNA-141 were used as interferences to evaluate the selectivity. As shown in the Figure 8C, the ECL responses of interference groups had similar results as the blank sample group. Meanwhile, the ECL intensities of the biosensor corresponding to the presence of target miRNA-21 (1 fM) or a mixture containing miRNA-21 and interferences (100 fM) were much higher than that of the blank sample group. Theses results proved that the constructed biosensor could specifically identify and detect miRNA-21. Finally, as depicted in Figure 8D, the stability of this biosensor was detected with 10 fM and 10 pM miRNA-21 under a continuous scan for 10 cycles, and the relative standard deviation (RSD) values were 0.75% and 0.61%, respectively. These results demonstrated that the biosensor showed outstanding stability.

Application. To measure the detection ability of the biosensor, it was used to detect the extracts of Hela cells and MCF-7 cells. As we can see from Figure 9, the corresponding ECL response also increased significantly when the number of MCF-7 cells increased, but the ECL intensity did not increase obviously with the growing number of Hela cells, which indicated that the expression of miRNA-21 in MCF-7 cells was higher than in Hela cells. Those results showed agreement with previous reports,[29,30] indicating that this constructed biosensor could be used to detect the expression of miRAN-21 in cancer cells.

CONCLUSIONS

In summary, we constructed an ultrasensitive biosensor platform for detection of microRNA-21 (miRNA-21) through graphitic carbon nitride with carbon vacancies (V_C-g-C_3N_4) as an ECL emitter and improved cascade strand displacement amplification (IC-SDA). Notably, carbon vacancies could enhance conductivity and adsorb coreaction reagent $S_2O_8^{2-}$ to promote its reduction, which could significantly improve ECL efficiency. Meanwhile, the target miRNA-21 could be transformed into a large amount of output DNA though IC-SDA to realize the ultrasensitive detection of miRNA-21 with a low LOD of 3.34 aM. Therefore, this work provided a new insight to improve the ECL efficiency of ECL emitters and

https://doi.org/10.1021/acs.analchem.2c02462
Anal. Chem. 2022, 94, 12444−12451

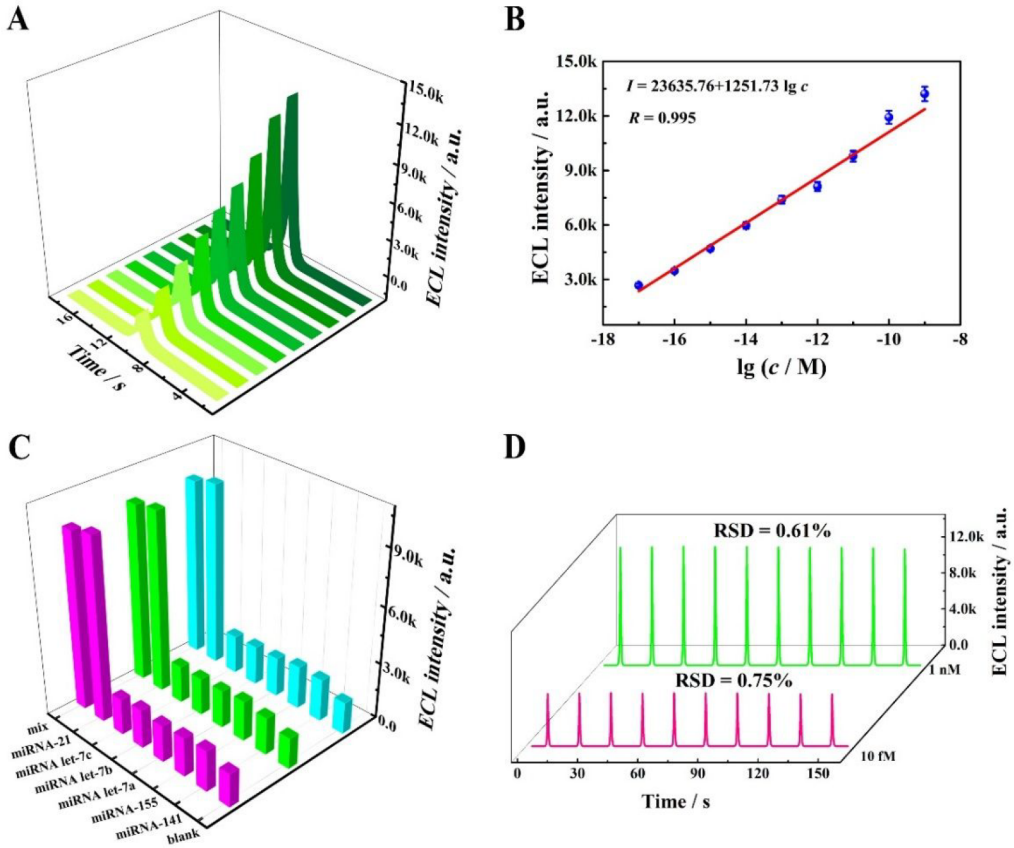

Figure 8. (A) ECL curves corresponding to different miRNA-21 concentrations. (B) Calibration curve for miRNA-21 analysis, n = 3. (C) Selectivity and (D) stability of the biosensor.

Table 1. Comparison of Various Methods for miRNA-21 Detection

analytical methods	linear range	LOD	ref
Electrochemistry	1 fM−100 pM	0.26 fM	23
Chemiluminiscence	40 fM−1 nM	10 fM	24
Fluorescence	1 fM−1 nM	0.86 fM	25
ECL	100 aM−100 pM	52.5 aM	26
ECL	10 fM− 0.1 nM	6.6 fM	27
ECL	10 fM−1 nM	8.19 fM	28
ECL	10 aM−1 nM	3.34 aM	This work

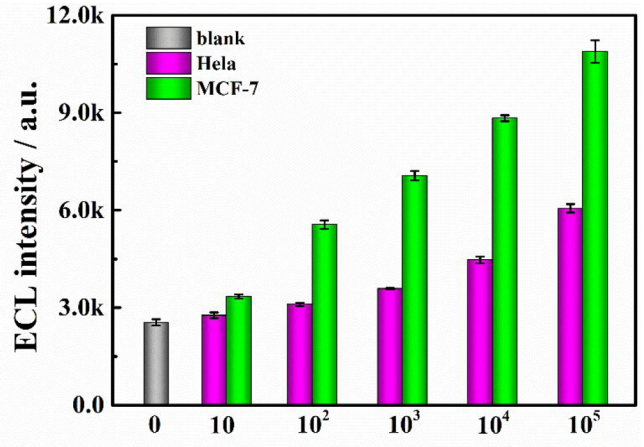

Figure 9. ECL analysis of this biosensor in extracts of Hela and MCF-7 cells.

construct biosensors for detection of biomolecules and diagnosis of disease.

■ ASSOCIATED CONTENT

Supporting Information

The Supporting Information is available free of charge at https://pubs.acs.org/doi/10.1021/acs.analchem.2c02462.

Reagents and materials, instruments, UV−vis, PL spectrum, FT-IR and XRD spectra, ECL efficiency of g-C_3N_4 and V_C-g-C_3N_4-50, ECL spectra of V_C-g-C_3N_4-x, characterization of biosensor construction process, and optimization of the testing condition (PDF)

■ AUTHOR INFORMATION

Corresponding Authors

Yaqin Chai − *Key Laboratory of Luminescence Analysis and Molecular Sensing, Ministry of Education Chongqing, College of Chemistry and Chemical Engineering, Southwest University, Chongqing 400715, People's Republic of China;* orcid.org/0000-0003-4392-9592; Phone: +86 23 68252277; Email: yqchai@swu.edu.cn; Fax: +86 23 68253172

Ruo Yuan − *Key Laboratory of Luminescence Analysis and Molecular Sensing, Ministry of Education Chongqing, College of Chemistry and Chemical Engineering, Southwest University, Chongqing 400715, People's Republic of China;* orcid.org/0000-0003-3664-6236; Email: yuanruo@swu.edu.cn

Authors

Linlei Liu − *Key Laboratory of Luminescence Analysis and Molecular Sensing, Ministry of Education Chongqing, College of Chemistry and Chemical Engineering, Southwest University, Chongqing 400715, People's Republic of China*

Yidan Zhu − *Key Laboratory of Luminescence Analysis and Molecular Sensing, Ministry of Education Chongqing, College of Chemistry and Chemical Engineering, Southwest University, Chongqing 400715, People's Republic of China*

Haijun Wang − *Key Laboratory of Luminescence Analysis and Molecular Sensing, Ministry of Education Chongqing, College of Chemistry and Chemical Engineering, Southwest University, Chongqing 400715, People's Republic of China;* orcid.org/0000-0002-6629-8407

Yue Zhang − *Key Laboratory of Luminescence Analysis and Molecular Sensing, Ministry of Education Chongqing, College of Chemistry and Chemical Engineering, Southwest University, Chongqing 400715, People's Republic of China*

Complete contact information is available at: https://pubs.acs.org/10.1021/acs.analchem.2c02462

Notes

The authors declare no competing financial interest.

■ ACKNOWLEDGMENTS

This work was financially supported by the NNSF of China (22174113, 22176153, and 21974108)

■ REFERENCES

(1) Kim, J. G.; Sun, J. Y.; Zhao, Y.; Wen, J. H.; Zhou, B.; Zhang, Z.; Mo, S. D.; Wang, J. L.; Liu, H. J.; Wang, G. C.; Yu, Q. L.; Liu, M. Y. *Small* **2022**, *18*, 2107807.

(2) She, X. J.; Zhu, X. W.; Yang, J. M.; Song, Y. H.; She, Y. B.; Liu, D. B.; Wu, J. J.; Yu, Q.; Li, H. M.; Liu, Z.; Ajayan, P. M.; Xu, H. *Nano Energy* **2021**, *84*, 105869.

(3) Xu, L. L.; Zhao, H. Y.; Sun, M. Z.; Huang, B. L.; Wang, J. W.; Xia, J. L.; Li, N.; Yin, D. D.; Luo, M.; Luo, F.; Du, Y. P.; Yan, C. H. *Angew. Chem., Int. Ed.* **2019**, *58*, 11491−11496.

(4) Du, Y.; Xue, J. W.; Sun, X.; Wu, D.; Liu, X. J.; Ju, H. G.; Yang, L.; Wei, Q. *Anal. Chem.* **2020**, *92*, 8472−8479.

(5) Feng, J. H.; Li, N.; Du, Y.; Ren, X.; Wang, X. Y.; Liu, X. J.; Ma, H. M.; Wei, Q. *Anal. Chem.* **2021**, *93*, 14196−14203.

(6) Xu, J. J.; Jiang, D. P.; Qin, Y. L.; Xia, J.; Jiang, D. C.; Chen, H. Y. *Anal. Chem.* **2017**, *89*, 2216−2220.

(7) Jiang, X. Y.; Wang, H. J.; Chai, Y. Q.; Shi, W. B.; Yuan, R. *Anal. Chem.* **2020**, *92*, 8992−9000.

(8) Wang, J.; Haghighatbin, M. A.; Shen, W.; Mi, L.; Cui, H. *Anal. Chem.* **2020**, *92*, 7062−7070.

(9) Zhu, L. P.; Yu, L. Y.; Meng, T.; Peng, Y.; Yang, X. R. *Small* **2021**, *17*, 2102881.

(10) Chen, L. C.; Zeng, X. T.; Si, P.; Chen, Y. M.; Chi, Y. W.; Kim, D. H.; Chen, G. N. *Anal. Chem.* **2014**, *86*, 4188−4195.

(11) Fan, Z. Q.; Lin, Z. Q.; Wang, Z. P.; Wang, J. F.; Xie, M. H.; Zhao, J. F.; Zhang, K.; Huang, W. *ACS Appl. Mater. Interfaces* **2020**, *12*, 11409−11418.

(12) Song, C.; Li, X. J.; Hu, L. H.; Shi, T. F.; Wu, D.; Ma, H. M.; Zhang, Y.; Fan, D. W.; Wei, Q.; Ju, H. X. *ACS Appl. Mater. Interfaces* **2020**, *12*, 8006−8015.

(13) Zou, R.; Lin, Y. J.; Lu, C. *Anal. Chem.* **2021**, *93*, 2678−2686.

(14) Du, X. J.; Jiang, D.; Dai, L. M.; Zhu, W. R.; Yang, X. D.; Hao, N.; Wang, K. *Anal. Chem.* **2018**, *90*, 3615−3620.

(15) Wang, X. Y.; Meng, J. Q.; Zhang, X. Y.; Liu, Y. Q.; Ren, M.; Yang, Y. X.; Guo, Y. H. *Adv. Funct. Mater.* **2021**, *31*, 2010763.

(16) Chu, K.; Li, Q. Q.; Liu, Y. P.; Wang, J.; Cheng, Y. H. *Appl. Catal. B: Environ.* **2020**, *267*, 118693.

(17) Jin, H. Y.; Li, L. Q.; Liu, X.; Tang, C.; Xu, W. J.; Chen, S. M.; Song, L.; Zheng, Y.; Qiao, S. Z. *Adv. Mater.* **2019**, *31*, 1902709.

(18) Liu, L. L.; Liu, Y. S.; Zhang, Y.; Yuan, R.; Wang, H. J. *Anal. Chem.* **2022**, *94*, 7191−7199.

(19) Zhang, X. L.; Liu, Y. H.; Du, S. M.; Yin, Y.; Kong, L. Q.; Chang, Y. Y.; Chai, Y. Q.; Li, Z. H.; Yuan, R. *Anal. Chem.* **2021**, *93*, 9568−9574.

(20) Li, Q.; Zhang, L. M.; Liu, J. N.; Zhou, J.; Jiao, Y. Q.; Xiao, X. D.; Zhao, C.; Zhou, Y.; Ye, S.; Jiang, B. J.; Liu, J. *Small* **2021**, *17*, 2006622.

(21) Wei, F. Y.; Liu, Y.; Zhao, H.; Ren, X. N.; Liu, J.; Hasan, T.; Chen, L. H.; Li, Y.; Su, B. L. *Nanoscale* **2018**, *10*, 4515−4522.

(22) Chen, A. Y.; Liang, W. B.; Wang, H. J.; Zhuo, Y.; Chai, Y. Q.; Yuan, R. *Anal. Chem.* **2020**, *92*, 1379−1385.

(23) Qi, T.; Song, C.; He, J.; Shen, W.; Kong, D. Z.; Shi, H. W.; Tan, L.; Pan, R. R.; Tang, S.; Lee, H. K. *Anal. Chem.* **2020**, *92*, 5033−5040.

(24) Chen, S. Y.; Zhao, J. J.; Xu, C. H.; Sakharov, I. Y.; Zhao, S. L. *Anal. Chem.* **2021**, *93*, 9218−9225.

(25) Wang, J.; Sun, J. Y.; Zhang, J.; Shen, C. L.; Zhang, X. L.; Xu, J. G. *Anal. Chem.* **2022**, *94*, 4437−4445.

(26) Liu, J. L.; Yang, R.; Chai, Y. Q.; Yuan, R. *Anal. Chem.* **2021**, *93*, 13334−13341.

(27) Ning, Z. Q.; Yang, E. L.; Zheng, Y. J.; Chen, M. Y.; Wu, G. Q.; Zhang, Y. J.; Shen, Y. F. *Anal. Chem.* **2021**, *93*, 8971−8977.

(28) Zhang, P.; Jiang, J.; Yuan, R.; Zhuo, Y.; Chai, Y. *J. Am. Chem. Soc.* **2018**, *140*, 9361−9364.

(29) Peng, L. C.; Yuan, Y. L.; Fu, X. M.; Fu, A.; Zhang, P.; Chai, Y. Q.; Gan, X. X.; Yuan, R. *Anal. Chem.* **2019**, *91*, 3239−3245.

(30) Kong, L. Q.; Kou, B. B.; Zhang, X. L.; Wang, D.; Yuan, Y. L.; Zhuo, Y.; Chai, Y. Q.; Yuan, R. *Chem. Sci.* **2021**, *12*, 15953−15959.